Ruh-Hua Wu[1]
Graduate Student
Department of Mechanical Engineering,
National Central University, Taiwan,
Republic of China
e-mail: wrh7215@ms7.hinet.net

Pi-Cheng Tung
Professor
Department of Mechanical Engineering,
National Central University, Taiwan,
Republic of China
e-mail: t331166@ncu.edu.tw

Fast Pointing Control for Systems With Stick-Slip Friction

A controller consisting of three schemes, one proportional gain, one pulse, and one ramp, is proposed to achieve precise and fast pointing control under the presence of stick-slip friction. Design of the controller is based on two distinctive features of friction, the varying sticking force and presliding displacement of contacts under static friction. The latter is the main idea behind the ramp scheme to accomplish the fast pointing task. Implementation of this multistage control strategy requires position measurement only. Experimental results demonstrate the effectiveness of the proposed controller for the desired performance. [DOI: 10.1115/1.1789977]

1 Introduction

Coulomb friction inherent in mechanisms poses a severe challenge to servomotor-controlled pointing systems. While approaching to the reference position, the system spends most of its movements either near or within the stuck regime, in which the controller has to provide particular efforts to eliminate the tiny errors caused by static friction. Unfortunately, friction in this regime is the most difficult part to model [1–3]. Many methods have been proposed to reduce the influence of friction on control systems, and these methods can be mainly divided into the model-based and the nonmodel-based approaches.

The model-based methods try to estimate the friction load and counteract it by the opposite control [1,3–5]. Some advanced approaches, such as robust schemes [6], variable structure [7], nonlinear identification and feedback [8], and accelerated evolutionary programming [9] have been reported. No matter what the control scheme is, the friction model is the core of these model-based methods. In early cases, the classical discontinuous model, or the so-called Coulomb friction model (Fig. 1), is employed due to its simplicity. This model, however, does not describe the friction force for zero velocity. Some static models have been proposed to handle this problem by adding parameters to describe friction at zero velocity [3]. For continuous models, Dahl proposed a first-order differential equation to describe friction [10]. Later Canudas de Wit et al. developed a well-known friction model, known as the LuGre model [11], which describes the average deflection of the bristles [12]. This model captures most phenomena caused by friction and soon became a widely adopted model for the model-based approaches [1,13,14]. But it has been pointed out that identifying this mode in the low-velocity regime is a difficult task [13]. To accomplish the identification requires a very stiff low-velocity-control loop [1,2]. Although the task is not easy, the model-based approach argues its value by removing the need for high-gain PI or PID controllers.

In contrast, the nonmodel-based approach applies various strategies to reduce the influence of friction without requiring its precise model. PI or PID types of controllers have been employed in industry for years because of their simplicity and robustness. In some systems, however, integral control suffers the hunting problem [11,15] and derivative control has to handle the noise in measurement. Using dither signals is a very popular, almost standard, technique for hydraulic servo actuators to reduce the impact of friction, but it is not recommended for electromechanical systems. As an alternative, impulsive control can reduce the sensitivity of the system to friction [3]. This scheme applies pulses to create a small displacement or a controlled breakaway, leading to transition to another control schemes [2,6,15–17]. However, except with an especially designed apparatus [18], it is not easy to precisely create the designed displacement [6,15–17]. Dual mode control integrates two modes of control in a single mechanism: gross motion in the regular way (macrodynamics) and fine motion in the range of presliding displacement (microdynamics) [19–21]. A typical problem with this control scheme is that intermediate motions, pointing distances that are outside the ranges of the macro and the micro dynamics, are difficult to accurately control [20].

In this paper, we propose a three-scheme controller, one proportional gain, one pulse, and one ramp (PPR), to achieve fast and precise pointing control for systems with friction. The pulse scheme is designed to break the possible stuck condition during reverse motion and thus shorten the transient period. The ramp scheme takes advantage of the elastic deformation of contacts under static friction to achieve μm-level pointing accuracy. The transition between schemes is determined simply by the error and the velocity of the system. Experimental results are presented to demonstrate the effectiveness of the proposed PPR controller.

The rest of this paper is arranged as follows: Section 2 presents the modeling and identification of the experimental system. Section 3 introduces the design of the PPR controller and discusses the stability. Experimental results are given in Sec. 4. Section 5 concludes this paper.

2 The Experimental System

Figure 2 gives the schematic and the block diagrams of the experimental system. Table 1 lists the notation and their estimates. Here we denote T_c as the Coulomb friction torque, T_s as the static friction torque, and T_f, the combination of T_c and T_s. T_{cf} in Fig. 1 stands for the Coulomb friction torque in the forward direction. Note that in Fig. 2(b) the viscous friction torque ($D\omega$) is included in the model of the plant while the friction load T_f is considered an external load.

In this system, two types of position sensors are available. One is the inductive displacement sensor (IDS) with 1-μm resolution and 2-mm measuring range. The other is the built-in encoder of the dc motor with 4000 pulses per revolution. In closed-loop tests, we take the position readings from the IDS, as shown in Fig. 2(a). In this configuration, the movement of the table is directly detected by the IDS and therefore positioning accuracy of μm level can be achieved under the existence of nonlinearities such as backlash, pitch error, thermal expansion, etc. On the other hand, in

[1]Author to whom correspondence should be addressed. P.O. Box 90008-15-15 Lung-Tan, Tao-Yuan 325, Taiwan, R.O.C. Phone: 886-3-4712201 ext. 356344; Fax: 886-3-4893874.

Contributed by the Dynamic Systems, Measurement, and Control Division of THE AMERICAN SOCIETY OF MECHANICAL ENGINEERS for publication in the ASME JOURNAL OF DYNAMIC SYSTEMS, MEASUREMENT, AND CONTROL. Manuscript received by the ASME Dynamic Systems and Control Division December 10, 2003. Associate Editor: M. Goldfarb.

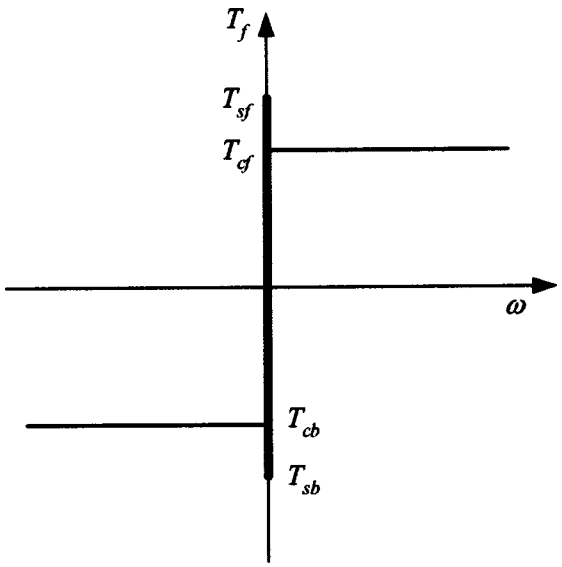

Fig. 1 The discontinuous Coulomb friction model, with the viscous part not shown

open loop tests used to identify the system, we take the position readings from the encoder. The latter types of tests run throughout the travel of the ball screw.

Most of the parameters listed in Table 1 can be obtained from the data sheet of the motor, except J and D, which are identified from the dynamics of the overall system. If all inertia is reflected to the motor shaft and the armature inductance L is neglected for its relatively small value, the transfer function from u to ω in Fig. 2(b) can be expressed as a first-order system

$$\frac{\Omega(s)}{U(s)}=\frac{K_TK_A}{RJs+K_BK_T+RD}=\frac{\frac{K_TK_A}{RJ}}{s+\frac{K_BK_T+RD}{RJ}} \tag{1}$$

without considering the friction load T_f. In addition, we assume that T_f is approximately constant if the velocity does not change sign (see Fig. 1). With this assumption, we designed a sequence of steps as the input u to estimate J and D without encountering reversion in the test.

By removing the dc components from the input and output data, we can obtain a first-order transfer function from u to ω, expressed as

$$\frac{\Omega(s)}{U(s)}=K\frac{p}{s+p} \tag{2}$$

Comparing Eq. (2) with Eq. (1) yields the estimates of J and D,

$$J=\frac{K_AK_T}{pRK};\quad D=\frac{K_T}{R}\left(\frac{K_A}{K}-K_B\right) \tag{3}$$

Figures 3 and 4 show the input u and the output ω obtained from the test data and the estimated model in Eq. (1), respectively. Conformity of the two types of data verifies the success of this approach to estimate the experimental system under the influence of friction.

The Coulomb friction torque T_c is estimated by collecting the steady state behavior of the system. Denoting u_{ss} and ω_{ss} as the steady state values of u and ω, and neglecting the dynamic terms in Fig. 2(b), we have

$$T_c=\frac{(u_{ss}K_A-\omega_{ss}K_B)K_T}{R}-D\omega_{ss} \tag{4}$$

The estimation of the static friction torque T_s here is made by recording the driving command u_m that starts to move the table,

$$T_s=\frac{u_mK_AK_T}{R} \tag{5}$$

The estimates of T_c and T_s are also given in Table 1. Note the distinct values of T_c and T_s in both directions. Although the value of T_s depends on several factors such as dwell time, position, temperature, lubrication, loading conditions, etc.; it can be simply considered a constant here. In designing the PPR controller, the estimation of T_s need not be very precise. It will be shown in Section 3.4 that the proposed control schemes are robust to changes of T_s.

3 Design of the PPR Controller

3.1 Principle of the Proposed Controller. The PPR controller is composed of three schemes, and Fig. 5 gives a block diagram of the system with the configuration of the controller illustrated. This controller uses the error (e) and the velocity ($\dot{y}$) to determine the transition between schemes. Here $\dot{y}$ is estimated by taking the first difference on the position signal,

$$\dot{y}(k)=\frac{y(k)-y(k-1)}{T} \tag{6}$$

where $y(k)$ is the position at the kth sample and T is the sampling interval. Although this may lead to some noise in $\dot{y}$ estimated by Eq. (6), the estimation acts as a threshold only to determine the state of motion and the design of the PPR controller does not require very precise estimation of $\dot{y}$. It will be clear that the control laws of the PPR controller do not contain derivative terms.

With the estimation of $\dot{y}$, the idea behind the PPR controller is stated as follows. The P scheme drives the system toward the target. As the system gets closer to the target, it must slow down, then becoming liable to get stuck due to the increase of friction in the very low-velocity regime [2,3]. If the system stops moving, it will not restart until the control effort rises to an adequate level to overcome the maximum static friction force. This delay in the start of movement is usually not desirable for fast pointing control. Intuitively, the use of pulses can avoid such delays because they can break the possible adhesion caused by static friction. Thus, when the PPR controller estimates that the velocity is low and the error is still large, it switches to the pulse scheme to start the movement. As the error becomes so small that the pulse may cause the system to slide over the target, the ramp scheme is activated. This scheme achieves the precise positioning task by manipulating presliding displacement. Figure 6 illustrates how the $\dot{y}$-e phase plane is divided into various regions for the three schemes and Fig. 7 depicts the flowchart of the PPR controller. Before introducing the design details, the condition of motion must be specified, as stated in Sec. 3.2.

3.2 Determination of Conditions of Motion. Because static friction behaves in a very different way from dynamic friction does, it is important for the PPR controller to distinguish the state of motion. Here we define that the system is in motion if

$$|\dot{y}|>V_s \tag{7}$$

otherwise it is in the sticking mode. Ideally, V_s would be zero but practically it is not. Due to the strong dependence of V_s on the frictional mechanism and conditions of measurement, we propose to search for V_s from experiments. Figure 8 shows one such experiment, in which the velocity approximately ranges from -0.05 to 0.05 mm/s in the sticking mode. Since further tests on the experimental system yield the same result, we set $V_s=0.05$ mm/s.

As stated in Sec. 3.1, taking the first difference on the position signal may lead to some noise, but the design of the PPR controller does not rely on very precise information of $\dot{y}$. It will be

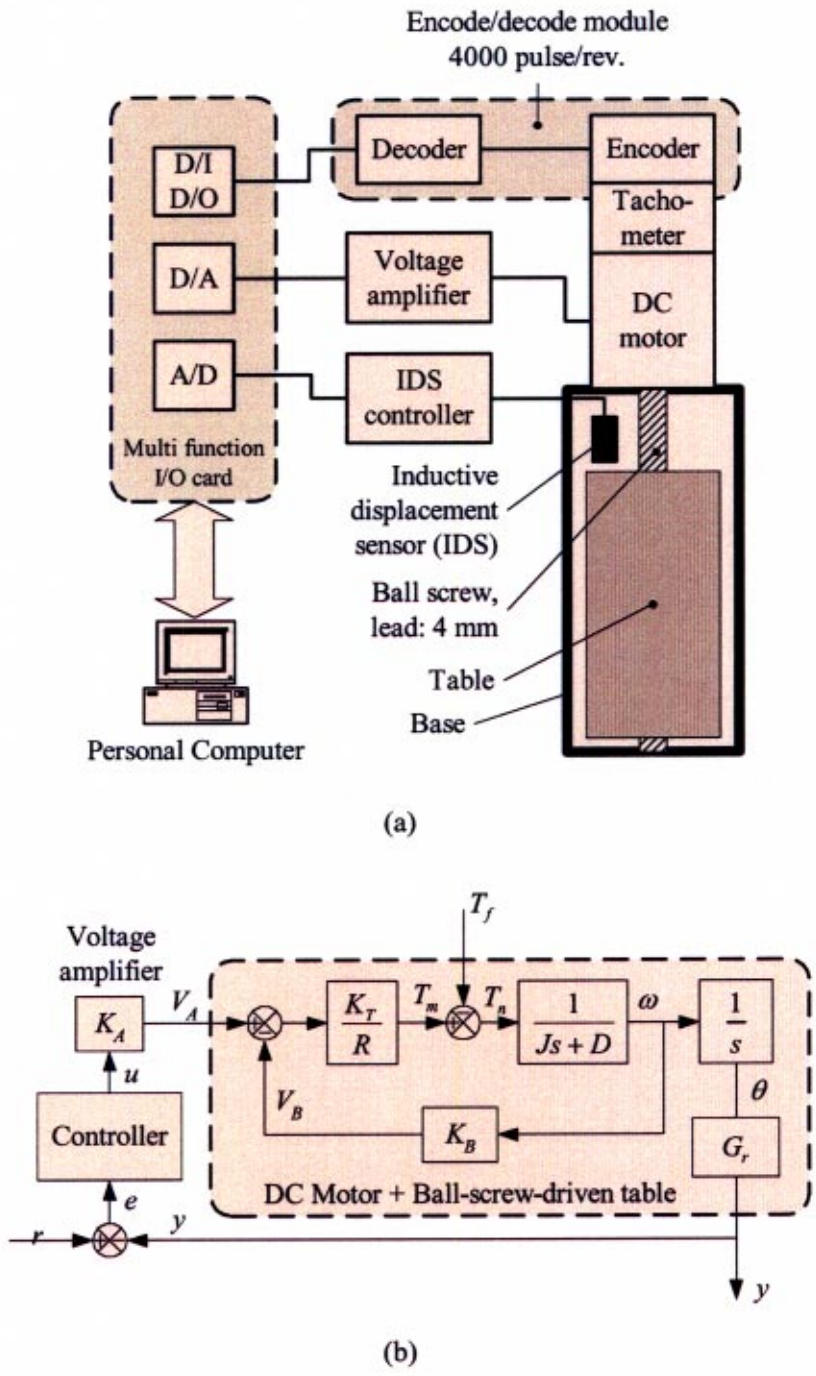

Fig. 2 The experimental system. (a) Schematic diagram. (b) Block diagram.

shown in experimental evaluations that, even though the estimate of velocity is noisy, as shown in Fig. 8, the proposed PPR controller can still achieve very precise and fast pointing control.

3.3 Region 0: Proportional-Gain Scheme. From Fig. 6, region 0 ($|\dot{y}|>V_s$) is the area in which the system is considered to be in motion. Since the influence of friction is not conspicuous unless the motion comes almost to a stop, it is not so necessary to compensate for Coulomb friction if the table is in motion. Therefore proportional-gain control is adopted in this region. Actually controllers of PD, PID, or any reasonable types can be candidates, but here the P controller is selected in order to demonstrate the simplicity and effectiveness of the proposed strategy. By neglecting the friction load T_f in Fig. 2(b), we can obtain the transfer function of the P-controlled system,

$$G_P(s)=\frac{Y(s)}{R(s)}=\frac{K_pK_AK_TG_r}{RJs^2+(K_BK_T+RD)s+K_pK_AK_TG_r} \quad (8)$$

where K_p is the gain of the P controller. Note that in Fig. 2(b) and Eq. (8), the armature inductance L is neglected for its relative small value. $G_P(s)$ in Eq. (8) is equivalent to

Table 1 Parameters of the experimental system

Symbol and name	Value	Unit	Source
D: viscous damping (motor+load)	50.46×10^{-3}, forward 13.85×10^{-3}, backward	N m/(rad/s)	Estimated from Fig. 3
G_r, gear ratio	$4/2\pi$	mm/rad	Ball screw lead 4 mm
J, moment of inertia (motor+ball screw)	2.02×10^{-3}	N m s^2	Estimated from Fig. 3
K_A, gain of voltage amplifier	19.88		Spec. of the voltage amplifier
K_B, back EMF constant of motor	0.278	V/(rad/s)	Spec. of the dc motor
K_T, torque constant of motor	0.278	N m/A	Spec. of the dc motor
L, armature inductance	1.1	mHenry	Spec. of the dc motor
K_s, tangential stiffness	72, forward 79, backward	N m/rad	Estimated from Fig. 12 and Eq. (24)
R, armature resistance	0.53	Ω	Spec. of the dc motor
T_c, Coulomb friction torque	+0.20, forward (T_{cf}) −0.41, backward (Tch)	N m	Estimated by Eq. (4)
T_s, maximum static friction torque	+0.44, forward (T_{sf}) −0.67, backward (Tsb)	N m	Estimated by Eq. (5)

$$G_P(s)=\frac{\omega_n^2}{s^2+2\zeta\omega_n s+\omega_n^2} \tag{9}$$

Choosing $K_p=1$ gives $\omega_n=9.15$ Hz and $\zeta=0.84$ for the forward motion and 0.69, backward. The distinct values of ζ result from the different viscous damping D in the two directions (see Table 1).

The control law in region 0 is simply

$$u=K_p e \tag{10}$$

With this control law, the friction-induced steady-state error e_{ss} can be expected. Equation (11) gives an estimate of e_{ss}

$$\frac{T_{sb}R}{K_pK_AK_T}=e_n\leqslant e_{ss}\leqslant e_p=\frac{T_{sf}R}{K_pK_AK_T} \tag{11}$$

where T_{sb} and T_{sf} are defined in Fig. 1. Substituting the values of T_{sb} and T_{sf} listed in Table 1 into Eq. (11) yields

$$-64\ \ \mu\text{m}\leqslant e_{ss}\leqslant 42\ \ \mu\text{m} \tag{12}$$

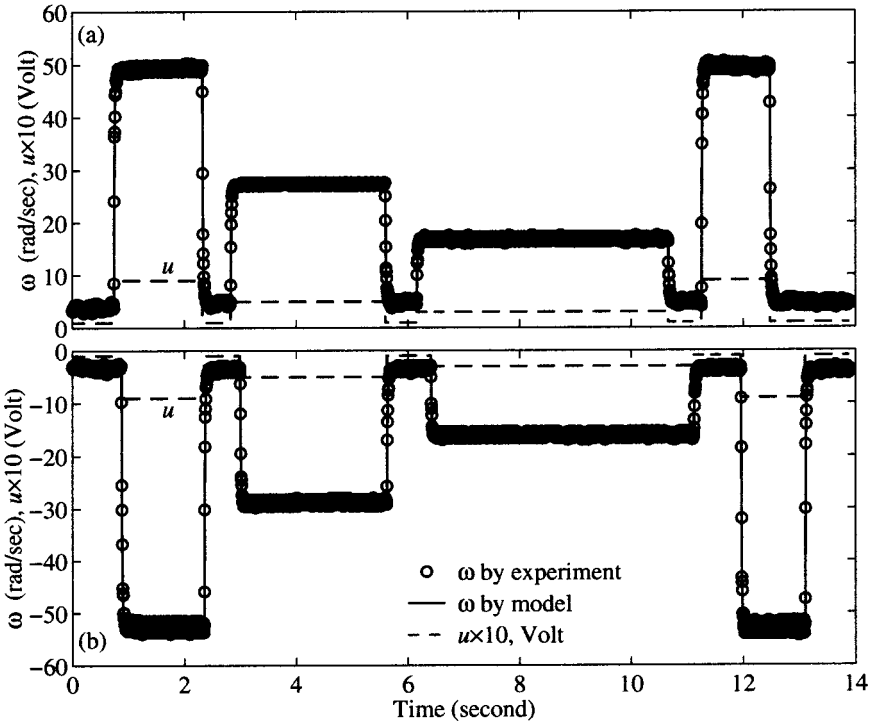

Fig. 3 Identification of the experimental system. (a) Test in the forward direction. (b) Test in the backward direction.

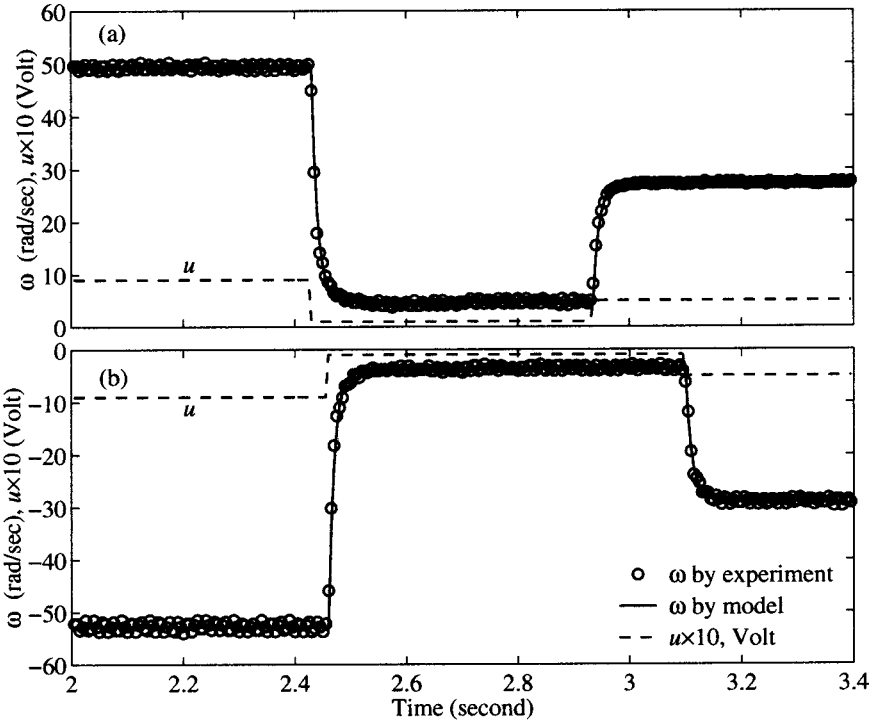

Fig. 4 Portions of the velocity profile shown in Fig. 3. (a) Test in the forward direction. (b) Test in the backward direction.

On the other side, the designed tolerance e_d in this paper is

$$-0.5\ \ \mu\text{m} = -E_{\text{II}} \leqslant e_d \leqslant E_{\text{II}} = 0.5\ \ \mu\text{m} \tag{13}$$

The E_{II} in Eq. (13) as well as in Fig. 6 is assigned according to the resolution of the position sensor. We will discuss the selection of E_{II} further in Sec. 3.6. When the gap between e_{ss} and e_d is large, further control is necessary to drive the system into the target specified in Eq. (13). Here we propose the pulse and the ramp signal for solutions, as described in Secs. 3.4 and 3.5.

3.4 Region I: Pulse Control Scheme. The design of the pulse scheme is based on two chief considerations. The first one is that the pulse shall be applied when the system stays in the sticking mode with an error larger than the designed tolerance E_{II}. On the other hand, it shall not be activated if the error is less than a critical value E_{I}. The design of E_{I} is to prevent the system from limit cycling about the command position. These two considerations specify region I in Fig. 6,

$$|e| > E_{\text{I}} \quad \text{and} \quad |\dot{y}| \leqslant V_s \tag{14}$$

The E_{I} in Eq. (14) is the error limit prohibiting the use of pulses. Determination of E_{I} requires the knowledge of presliding displacement (see Sec. 3.5).

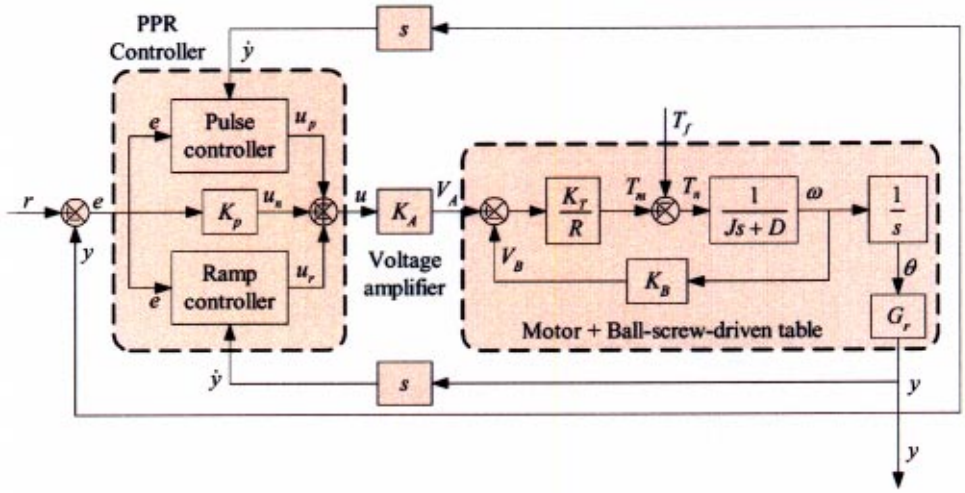

Fig. 5 Block diagram with the outline of the PPR controller

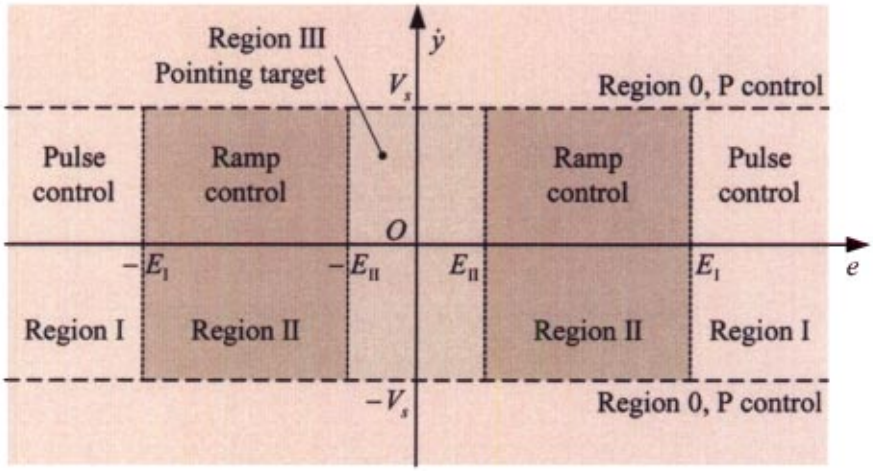

Fig. 6 PPR control schemes in the $\dot{y}-e$ phase plane

The control law in region I is

$$u = K_p e + u_p = K_p e + u_{\mathrm{PL}}\,\mathrm{sign}(e) \tag{15}$$

where u_{PL} is the pulse level. The width of a single pulse is equal to the sampling interval T. Several methods have been proposed to calculate the proper shape of the pulse [6,15,17], and these approaches assume that identical pulses generate the same displacement. Our experiments, however, reveal a different situation. Responses to the same pulse command u_p given at four different positions are compared in Fig. 9, which clearly exhibits the variation in the pulse responses. Further tests on the experimental system are shown in Figs. 10 and 11, giving the relations between the displacement and the pulse width, and those between the displacement and the pulse level, respectively. The results shown in Figs. 9–11 reveal that the deviation in pulse responses is large and thus suggest that algorithms for calculating the pulse shape are not necessary.

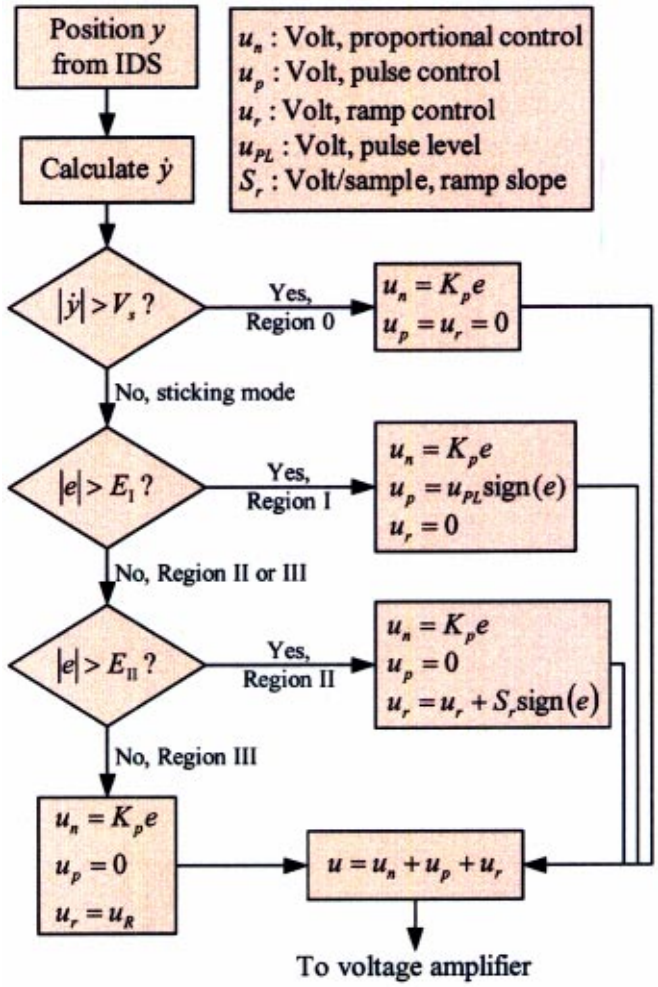

Fig. 7 Flowchart of the PPR controller

Therefore we design the pulse scheme to break static friction so that the system can continue moving before it reaches the target, not to create a movement of precise distance that, in the authors' opinion, is not accomplishable for most practical servo systems. Knowing that the control voltage u_m needed to overcome T_s is about 0.05 V [from Eq. (5) and Table 1], we choose $u_{\mathrm{PL}} = 0.1$ V, 2 times of u_m. Note that although T_s depends on factors like load, position, lubrication, temperature, dwell time, etc. [3]; the design here allows a large variations in T_s and u_m.

Although the design of a fixed u_{PL} seems simple, choosing a proper level of u_{PL} still calls for deliberation to handle the uncertainties in practical situations. On the one hand, pulses of higher levels can produce larger displacement but also larger variation, which implies higher risk of pulse-induced oscillations around the target. And on the other hand, it can be seen from Figs. 10 and 11 that low-level pulses with brief durations may not bring about any effective movement. This means that the energy developed by the pulse is not enough to break the adhesion in the sticking interface and translate the system from rest into motion.

The dilemma stated above is resolved by the unique variable-width feature of the pulse scheme. The principle behind this feature is simple. Although the width of a single pulse is equal to one sampling interval, successive pulses naturally form a wilder pulse. For example, if the pulse at the current sample does not create any effective movement, then the velocity is still low ($|\dot{y}| \leq V_s$), the states $(e, \dot{y})$ still remain in region I, the pulse at the next sample will be activated, and thus the width of the pulse is doubled. In this way, pulses of various widths with an increment of the sampling interval can be generated with no complicated algorithm. This unique feature will be demonstrated in the experimental evaluations.

3.5 Region II: Ramp Control Scheme. As mentioned in Sec. 3.4, the pulse scheme is not designed to complete the point-

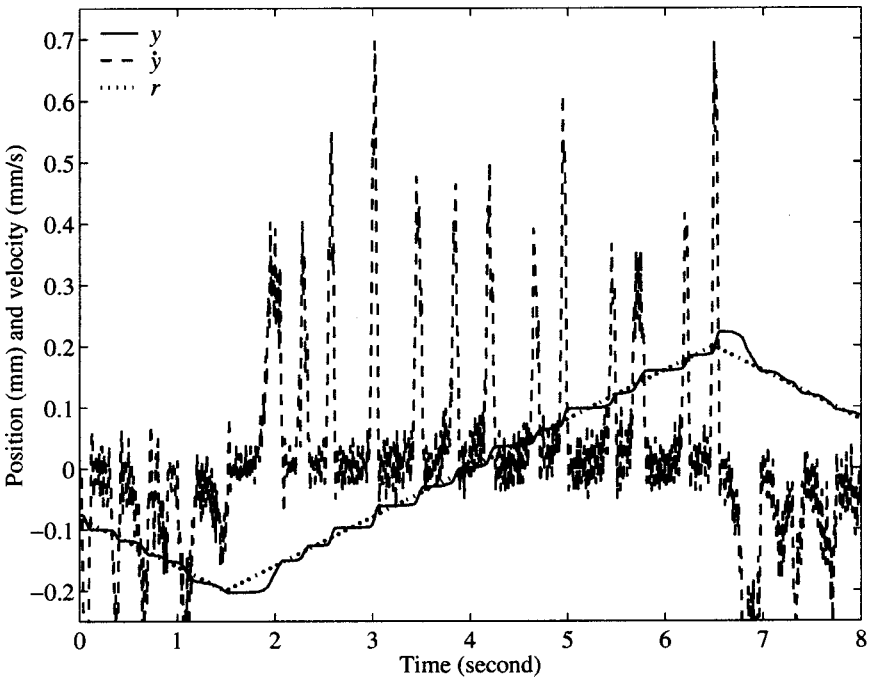

Fig. 8 A tracking test using a PI controller, $K_p=1$ and $K_i=5$, to determine V_s

ing task, but to drive the system to some locations close enough to the target so that the ramp scheme can proceed. At these locations the pulse is not suitable to be applied again due to the uncertainties shown in Figs. 10 and 11. The union of such locations is defined as region II in Fig. 6,

$$|\dot{y}| \leqslant V_s \quad \text{and} \quad E_{\mathrm{II}} < |e| \leqslant E_{\mathrm{I}} \tag{16}$$

In this region, we propose the ramp scheme to achieve fast and precise pointing control. The control law is

$$u = K_p e + u_r = K_p e + \mathrm{sign}(e) \int_0^t S_r d\tau \quad 0 < t \leqslant T_r, \quad S_r \geqslant 0 \tag{17}$$

where u_r is the ramp command, S_r is the slope of the ramp in V/sample, and t denotes time. T_r is the time specified for the ramp command to accomplish the pointing task. In this paper, the ramp slope S_r is designed to be a constant. Then u_r Eq. (17) can be represented by

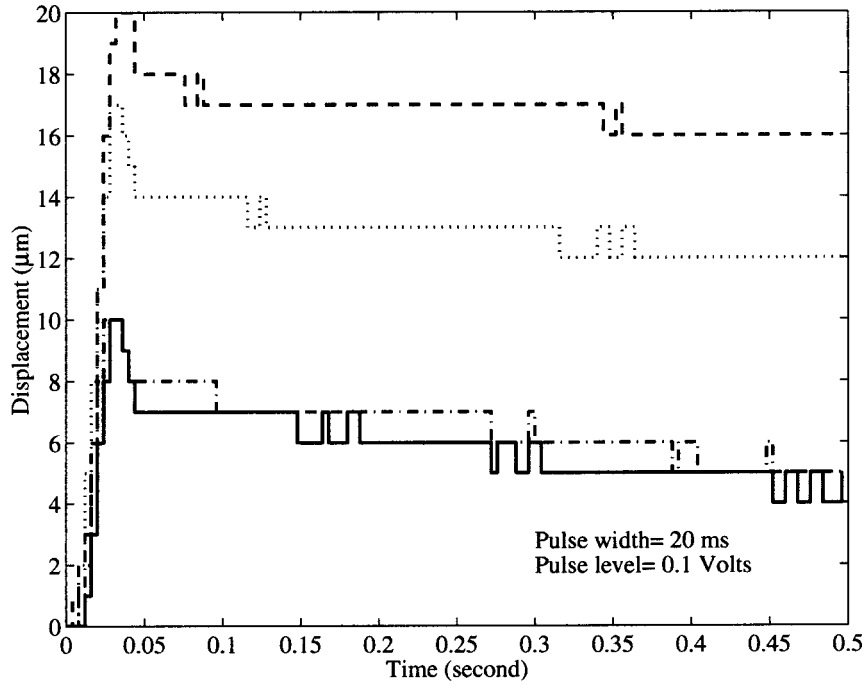

Fig. 9 Variation of the responses to identical pulses

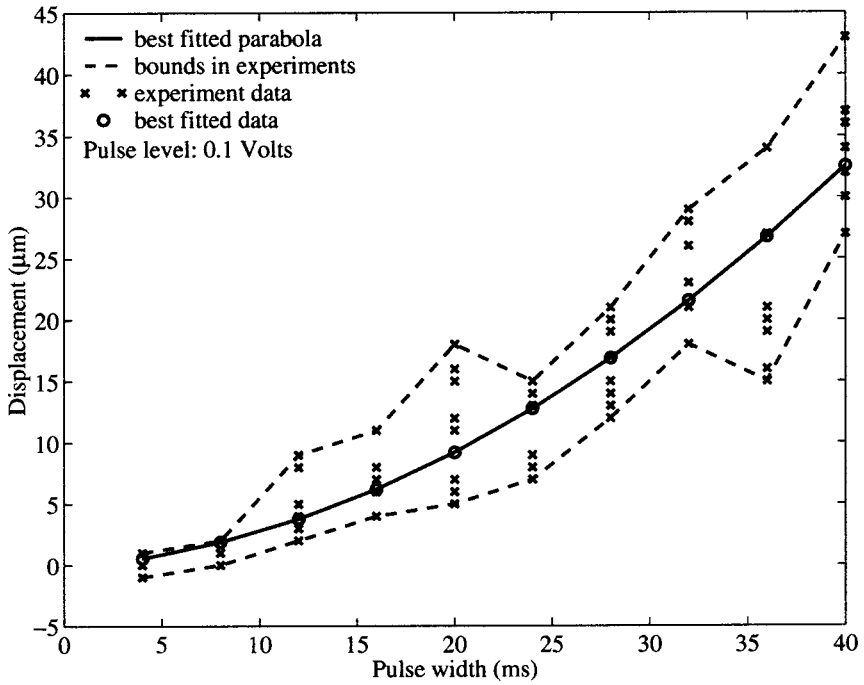

Fig. 10 Variations of the responses generated by pulses of different widths

$$u_r = \text{sign}(e) S_r t, \quad 0 < t \leq T_r, \quad S_r \geq 0 \tag{18}$$

Here Eq. (18) is implemented by

$$u_r(k) = \text{sign}[e(k)] S_r + u_r(k-1) \tag{19}$$

The control law given in Eq. (17) is inspired by the microscopic movement, referred to as presliding displacement, between contacts under static friction. In what follows we analyze the characteristics of the system in region II, introduce the details for designing the ramp controller, and demonstrate how this scheme accomplishes the fast and precise pointing task.

3.5.1 Presliding Displacement in Region II. It is known that in mechanics the asperities of contacts between surfaces act like micro springs when the tangential load is balanced by static friction [23,22]. The deflection of asperities in the interface results in presliding displacement, and this displacement, typically ranging from 2 to 5 μm, gives rise to the static friction force. That is, in the absence of fully developed sliding, friction is a force of constraint [23,24]. When the applied force exceeds the maximum static friction level, the balance collapses, breakaway occurs, and

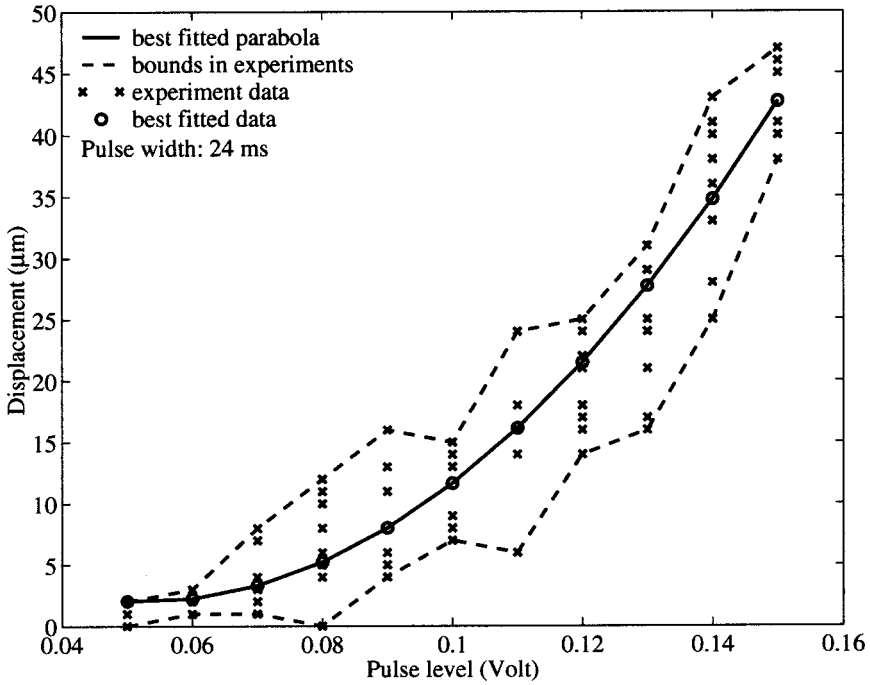

Fig. 11 Variations of the responses generated by pulses of different heights

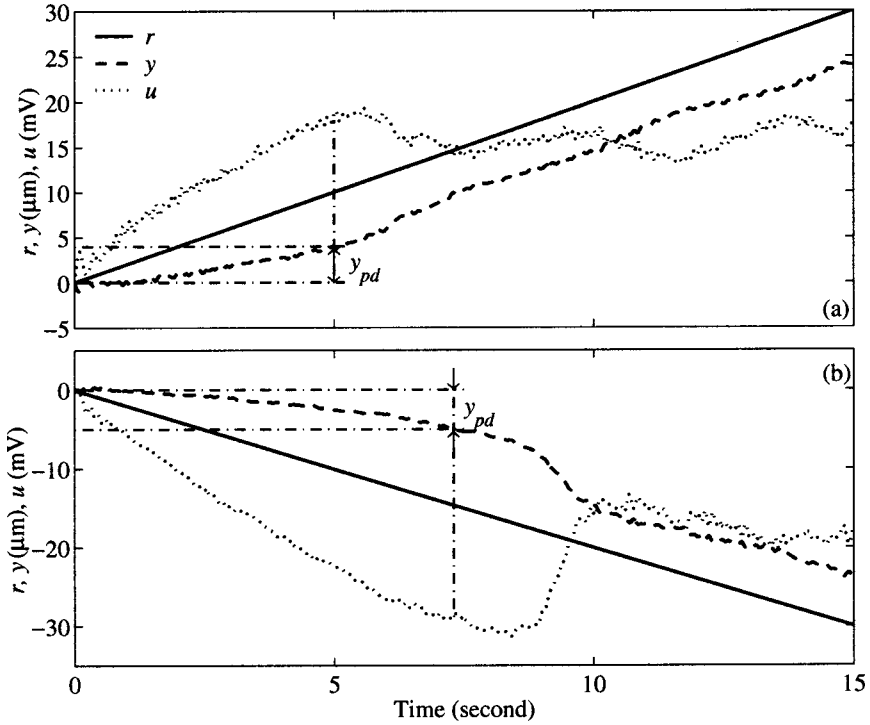

Fig. 12 Measurement of presliding displacement. (a) Forward direction. (b) Backward direction.

sliding starts. The effect of control action upon presliding displacement is crucial to pointing systems of very high accuracy.

Here we derive the relation between presliding displacement y_{pd} and the control u_r in the ramp scheme. Since the velocity $\dot{y}$ in the sticking mode is smaller than V_s, it can be reasonably neglected. From the block diagram shown in Fig. 2(b), we have

$$T_n = T_m - T_f = 0 \tag{20}$$

and

$$T_m = T_f = \frac{u_r K_A K_T}{R} \tag{21}$$

Next, we adopt the linear spring model for contacts under static friction [3]. The model is

$$K_s \theta_{\mathrm{pd}} = T_f \tag{22}$$

where K_s is the tangential stiffness of contacts and θ_{pd} is the angular presliding displacement. After converting θ_{pd} into the linear displacement y_{pd} by

$$\theta_{\mathrm{pd}} G_r = y_{\mathrm{pd}} \tag{23}$$

we have

$$y_{\mathrm{pd}} = \frac{K_A K_T G_r}{R K_s} u_r \tag{24}$$

The model in Eq. (22) can be justified by the observations presented in Fig. 12. The curves in this figure are obtained by giving a position command r of slope=2 μm/s and using a P controller with $K_p = 3$ to drive the closed-loop system. In Fig. 12, the range of presliding displacement is estimated to be about 4 μm in the forward direction and 5 μm, backward. Since the ramp scheme is designed to work in the sense of force balance, the error range of region II should not exceed that of presliding displacement to avoid abrupt slips as the ramp is pushing the table. From this consideration, we choose $E_{\mathrm{I}} = 3$ μm. The value of E_{II} is dependent on the resolution of the sensor and is set to be 0.5 μm. Further discussion on E_{II} is given in Sec. 3.6.

With presliding displacement introduced, we now describe how the ramp scheme achieves precise pointing control and why it is fast. The pulse scheme propels the system around the target with an error less than the range of presliding displacement. By balancing static friction and taking advantage of presliding displacement, the ramp controller drives the system until it moves into the target region. After that, the ramp command is fixed to keep the system there. The pointing task can be completed quickly because the ramp command has a constant rate of change, not an exponentially decaying rate, as the error approaches zero. If the integrator instead of the ramp scheme is used, its gain must be high enough to eliminate an error of several micrometers within a short period. Otherwise, the settling time will become quite long. Such a situation indeed has to do with the change in plant dynamics between the sliding and the sticking conditions, as analyzed below.

For a PID controller, since the error and the velocity in the sticking mode are very small, the proportional and derivative control efforts can be neglected. That is

$$u = K_p e + \int K_i e dt + K_d \frac{de}{dt} \cong \int K_i e dt \tag{25}$$

By Eqs. (21)–(25), the block diagram in Fig. 2(b) can be simplified into a first-order linear system with dynamics of the motor ($\dot{\theta}$ and $\dot{\omega}$) neglected, as shown in Fig. 13. In Fig. 13, the closed-loop transfer function $C(s)$ is

$$C(s) = \frac{Y_{\mathrm{pd}}(s)}{R(s)} = \frac{p}{s+p} \tag{26}$$

and the time constant τ_e of this first-order system is

$$\tau_e = \frac{1}{p} = \frac{R K_s \pi}{K_i K_A K_T 2} \tag{27}$$

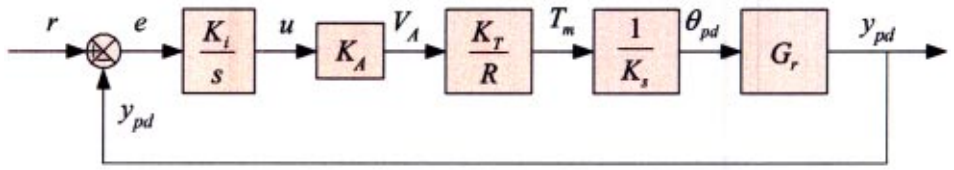

Fig. 13 The simplified model of the PID-controlled experimental system in the sticking mode

The value of K_s in Eq. (27) is determined from the data depicted in Fig. 12, which gives the measures of y_{pd} and u_r, as derived in Eq. (24). By substituting the values in Table 1, we get the estimation of K_s in Eq. (24) to be 72 N m/rad for the forward direction and 79 N m/rad, backward. Here we take the average of K_s to estimate τ_e in Eq. (27) and get the result $\tau_e = 1.12$ s when $K_i = 10$. For systems with stiffer frictional structures, the value of K_s can be the order of 10^3 N m/rad and the corresponding τ_e in Eq. (27) becomes even larger. The phenomenon of this integrator-induced slow dynamics in the sticking state can be observed in the experimental evaluations presented in Sec. 4.

3.5.2 Slope of the Ramp. The ramp scheme is characterized by its slope S_r. Suppose F_s is the sampling rate (Hz) and T_r is the time for the ramp scheme to complete the pointing task [see Eq. (17)]. Then in $F_s T_r$ samples the ramp has to reach u_m, the control that generates the torque to counteract T_s in Eq. (5). Thus we have

$$S_r = \frac{u_m}{F_s T_r} \text{ V/sample} \tag{28}$$

For example, suppose u_m is 50 mV, F_s is 250 Hz, and T_r is set to be 0.2 s. That is, we hope the table can reach the target within 0.2 s from any point in region II. Then Eq. (28) gives

$$S_r = \frac{50}{250 \times 0.2} = 1 \text{ mV/sample} \tag{29}$$

Equation (29) implies that in the ramp scheme, the control is changed by 1 mV at every sampling instant until the pointing task is done. The ramp control u_r in Eq. (17) is then fixed to keep the system in the target region.

3.6 Region III: Target Region. The target region or region III is defined by

$$|e| \leqslant E_{\mathrm{II}} \quad \text{and} \quad |\dot{y}| \leqslant V_s \tag{30}$$

The control law in this region is

$$u = K_p e + u_R \tag{31}$$

where u_R is the ramp command at the sample when the system reaches region III, a region bounded by E_{II} and V_s. Similar to the case of V_s, ideally E_{II} is zero but practically it is not. In this study, E_{II} is assigned according to the resolution of the position sensor (1 μm), that is, $E_{\mathrm{II}} = 0.5\ \mu$m. This setting, however, does not imply that the positioning accuracy can be always equal to the limit of the resolution of the sensor. In practice, factors like measurement noise, performance of the power amplifier, and experiment conditions should be considered. Similar to the case in sliding mode control, a tight target region for the PPR controller is likely to induce chattering around the reference position.

The design of the PPR controller is introduced above. In summary, two parameters of friction, the ranges of presliding displacement, from which E_{II} is determined, and the static friction torque, which specifies the pulse level u_{PL}, are essential to the design task. Table 2 summaries the parameters of the PPR controller designed for the experimental system.

3.7 Issues on Stability. In this section, the stability of the PPR controller is investigated from an engineering viewpoint. Although a solid proof is not given here, the authors believe that the following analysis can provide a good understanding to judge the stability of the proposed controller.

In region 0, the stability of the P-controlled system is guaranteed, as revealed in Eq. (8). In addition, the region

$$R_{a0} = \{(e, \dot{y}) | e_n \leqslant e \leqslant e_p, |\dot{y}| \leqslant V_s\} \tag{32}$$

is the attraction set for the states in region 0, where e_n and e_p are defined in Eq. (11).

The stability of the pulse scheme relies on the pulse level u_{PL}. If the torque created by the pulse is only slightly larger than the maximum static friction torque, then from the control law designed in Eq. (15) it can be asserted that region II and region III are the regions of attraction for all states in region I because of the very small movement caused by the pulse. On the other hand, if a high-level pulse generates a movement larger than $2E_{\mathrm{I}}$, the system may have a chance to slide over the target and reach region I on the other side of the reference position. Consequently oscillations around the target may occur due to the intermittent pulse command. Thus a lower pulse level benefits the stability of the pulse scheme at the cost of a longer transient period, whereas a higher one yields faster performance at the risk of limit cycling. Determination of the pulse level is thus a compromise between stability and performance. Achieving an optimal design is difficult due to the variation in the pulse responses shown in Figs. 10 and 11.

The ramp scheme is applied in a region bounded by E_{I} and E_{II} and its stability is partially dependent on the selection of these two parameters, as described in Secs. 3.5.1 and 3.6, respectively. In addition, the ramp slope S_r is also related with the stability of the

Table 2 Summary of the RRP controller

Region	Condition	Control law	Parameter
0	$\lvert\dot{y}\rvert > V_s$	Proportional-gain control: $u = K_p e$	$V_s = 0.05$ mm/s $K_p = 1$ V/mm
I	$\lvert e\rvert > E_{\mathrm{I}}$ and $\lvert\dot{y}\rvert \leqslant V_s$	Pulse control: $u = K_p e + u_{\mathrm{PL}}\,\mathrm{sign}(e)$	$E_{\mathrm{I}} = 3\ \mu$m $u_{\mathrm{PL}} = 0.1$ V
II	$E_{\mathrm{II}} < \lvert e\rvert \leqslant E_{\mathrm{I}}$ and $\lvert\dot{y}\rvert \leqslant V_s$	Ramp control: $u = K_p e + S_r\,\mathrm{sign}(e)t$	$E_{\mathrm{II}} = 0.5\ \mu$m $S_r = 1$ mV/sample
III	$\lvert e\rvert \leqslant E_{\mathrm{II}}$ and $\lvert\dot{y}\rvert \leqslant V_s$	$u = K_p e + u_R$	u_R: see Eq. (31)

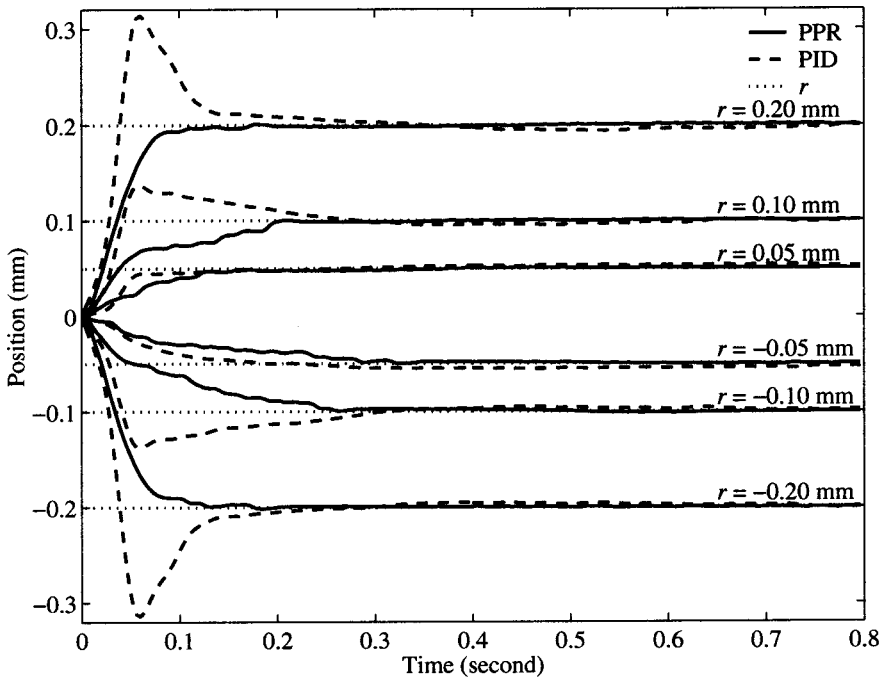

Fig. 14 Responses to various input steps

PPR controller. Applying a slight slope ensures the stability of the ramp controller because the dynamics of the system can be neglected in slow motion, as derived in Eqs. (20)–(24). Although using a steep slope may involve the dynamics of friction, the dissipative property of friction would be a great benefit rendering the stability of the ramp scheme.

Although a solid proof is not given here, its stability is demonstrated from the engineering-viewpoint analysis described above, as well as by the experimental evidences presented below.

4 Experimental Results

The proposed PPR controller is evaluated on the system introduced in Sec. 2. Since the undamped natural frequency of the P-controlled system is lower than 10 Hz [Eq. (9)], the sampling rate F_s is set to be 250 Hz.

Figure 14 depicts the step responses of the system and Fig. 15, the control efforts. Steps of different levels (0.05, 0.1, and 0.2 mm) are designed to investigate the influence of friction on the

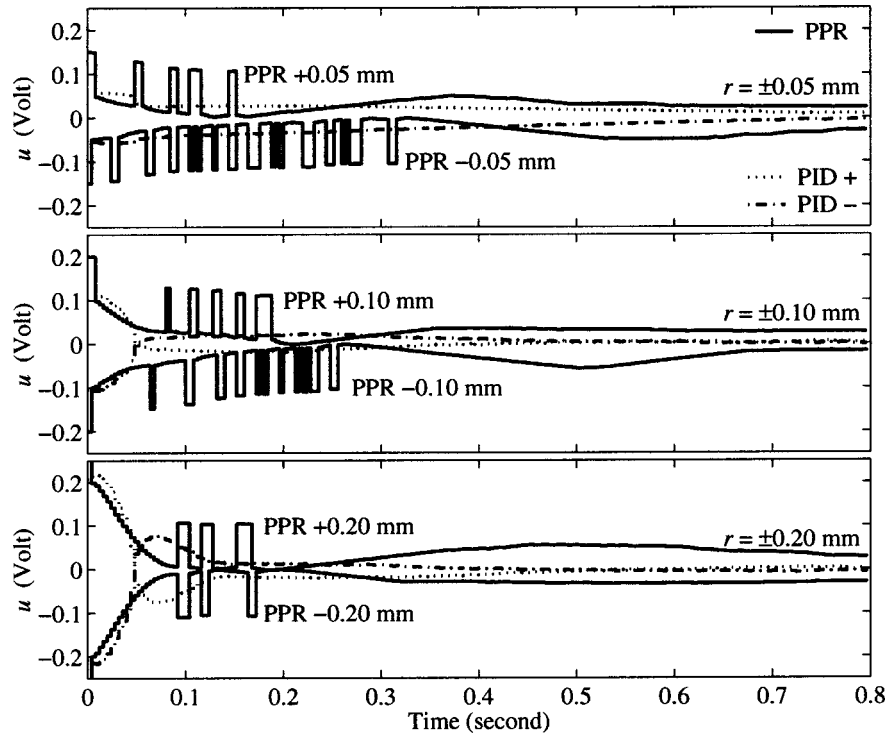

Fig. 15 Control efforts of the step responses shown in Fig. 14

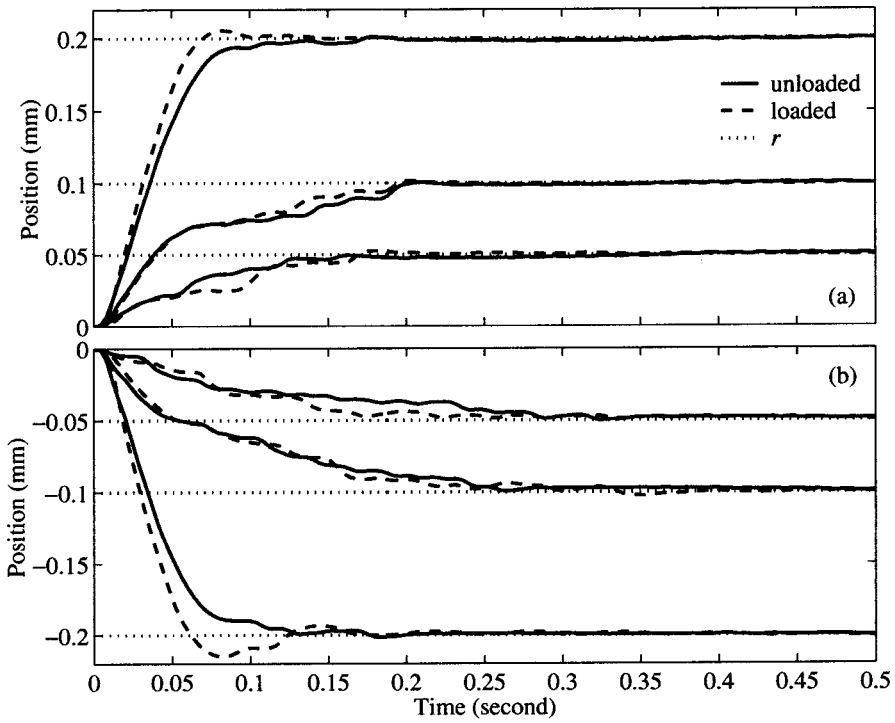

Fig. 16 Robust test of the PPR controller. (a) Positive command. (b) Negative command.

pointing performance. Responses and control efforts obtained by using a PID controller are also given in Figs. 14 and 15 for comparison. With regard to the PID controller, we designed one for the linear system without friction [Eq. (9)] but found that its performance is not satisfactory in experimental evaluations. Therefore we searched the following 80 candidates for the best combination: $K_p=[0.5,1,2,3]$, $K_i=[0,5,10,20]$, and $K_d=[0,0.001,0.003,0.005,0.01]$. The results are $K_p=1$, $K_i=10$, and $K_d=0.003$.

In testing the PID controllers, conspicuous overshoots (10%–60% in Fig. 14) were found to be unavoidable if a settling time less than 1 s is desired. In addition to the overshoot, long-lasting errors of two or three micrometers were also observed. Actually, this best-tuned PID controller did not finish the tasks until about 1.5–2 s, depending on the pointing distances. The cause of such slow dynamics has been analyzed in Sec. 3.5.1. In contrast, the PPR controller demonstrates both fast and precise pointing performance, with most of the tasks accomplished within 0.5 s without overshoot. Note the pulses of various widths in Fig. 15, which reveals the variable-width feature of the pulse scheme introduced in Sec. 3.4.

A test for the robustness of the PPR controller is presented in Fig. 16. In this test the table is loaded with a 20-kgw block and the PPR controller designed for the unloaded system is used. The identification on the friction parameters reveals that this load increases T_s and T_c (see Table 1) by about 12% and 5%, respectively. The damping coefficient D and the moment of inertia J are altered about 2% by this load. Although the change of D and J caused by this load is not much, the robustness of the PPR controller has been demonstrated through the distinct values of D, T_s, and T_c in both directions. It can be seen from Table 1 and Fig. 14 that the PPR controller allows at least a 50% variation in T_s and T_c. The tolerance of the proposed controller for D is even larger.

In addition to the satisfactory performance presented in Figs. 14 and 16, one important feature of the ramp scheme is also noticeable. It can be noted in Fig. 15 that a second ramp arises at about 0.5 s in the -0.1-mm step test. By a close inspection we found a microscopic slip occurs at the end of the first ramp. That is, the table did not stop at the end of the first ramp but overran the target by about 1 μm. This event triggered the second ramp and drove the system back to the target within 0.2 s. We found from other tests that it takes about 5 times longer for the PID controller to correct the same error. Due to the peculiar nonlinearity of friction in the stuck condition, we believe that it is very difficult to prevent such microscopic slips from occurring during the high-accuracy pointing processes. However, as revealed in the experimental results, the dissipativity of friction renders the ramp controller stable.

5 Conclusions

In this paper, a controller consisting of proportional-gain, pulse, and ramp schemes has been proposed to accomplish precise and fast pointing control under the presence of stick-slip friction. Each of the schemes, particularly the ramp scheme, was designed in accordance with the special features of stick-slip friction in various regimes. We have analyzed the property of this particular scheme in eliminating the very tiny error caused by static friction and demonstrated its performance through experimental evaluations. In such evaluations, using the PPR controller could accomplish pointing tasks of various distances with up to 1-μm accuracy and without overshoot, whereas using the best-tuned PID controller inevitably suffered from 10% to 60% overshoots and took at least 2 times longer than the PPR controller to finish the task. Furthermore, although in different directions the experimental system were found to have at least 50% variation in the friction parameters, the PPR controller still demonstrated uniform performance in the two directions.

Our future research will first concentrate on the stability proof of the proposed controller. Applying the variable pulse level in the pulse scheme to reduce the transient period further is also a future topic. In addition, we believe that if some more advanced algorithm can be integrated in the ramp scheme to handle the peculiar nonlinearity of friction in the sticking state, the performance of

the PPR controller can be further improved. Finally, the application of the PPR controller to a vertical positioning table has also been scheduled in our future study.

Acknowledgments

The authors are very grateful to the corresponding editor and reviewers, whose comments have significantly improved the quality of this paper. The financial support from the National Science Council (NSC) is also highly appreciated.

References

[1] Swevers, J., Al-Bender, F., Ganseman, C. G., and Prajogo, T., 2000, ''An Integrated Friction Model Structure With Improved Presliding Behavior for Accurate Friction Compensation,'' IEEE Trans. Autom. Control, **45**, pp. 675–686.

[2] Armstrong-Hélouvry, B., 1993, *Control of Machines With Friction*, edited by Norwell, Kluwer.

[3] Armstrong-Hélouvry, B., Dupont, P., and Canduas de Wit, C., 1994, ''A Survey of Models, Analysis Tools and Compensation Methods for the Control of Machines With Friction,'' Automatica, **30**, pp. 1083–1138.

[4] Canudas de Wit, C., Noël, P., Aubin, A., and Brogliato, B., 1991, ''Adaptive Friction Compensation in Robot Manipulators: Low Velocities,'' Int. J. Robot. Res., **10**, pp. 189–199.

[5] Canudas de Wit, C., Astrom, K. J., and Braun, K., 1987, ''Adaptive Friction Compensation in DC-Motor Drives,'' IEEE J. Rob. Autom., **RA-3**, pp. 681–685.

[6] Southward, S. C., Radcliffe, C. J., and MacCluer, C. R., 1991, ''Robust Nonlinear Stick-Slip Friction Compensation,'' ASME J. Dyn. Syst., Meas., Control, **113**, pp. 639–645.

[7] Guzzella, L., and Glattfelder, A. H., 1992, ''Pointing of Stick-Slip Systems Comparison of a Conventional and a Variable-Structure Controller Design,'' *Proc. 1992 American Control Conference*, Vol. Wp13, pp. 1277–1281.

[8] Johnson, C. T., and Lorenz, R. D., 1992, ''Experimental Identification of Friction and Its Compensation in Precise, Position Controlled Mechanisms,'' IEEE Trans. Ind. Appl., **28**, pp. 1392–1398.

[9] Kim, J. H., Chae, H. K., Jeon, J. Y., and Lee, S. W., 1996, ''Identification and Control of Systems With Friction Using Accelerated Evolutionary Programming,'' IEEE Trans. Control Syst. Technol., **16**, pp. 38–47.

[10] Dahl, P. R., 1977, ''Measurement of Solid Friction Parameters of Ball Bearings,'' in *Proc. of 6th Annual Symp. On Incremental Motion, Control Systems and Devices*, University of Illinois, ILO.

[11] Canudas de Wit, C., Olsson, H., Åström, K., and Lischinsky, P., 1995, ''A New Model for Control of Systems With Friction,'' IEEE Trans. Autom. Control, **40**, pp. 419–425.

[12] Haessig, D. A., and Friedland, B., 1991, ''On the Modeling and Simulation of Friction,'' ASME J. Dyn. Syst., Meas., Control, **113**, pp. 345–362.

[13] Canudas de Wit, C., and Lischinsky, P., 1997, ''Adaptive Friction Compensation With Partially Known Dynamic Friction Model,'' Int. J. Adapt. Control Signal Process., Vol. II, pp. 65–80.

[14] Bonsignore, A., Ferretti, G., and Magnani, G., 1999, ''Analytical Formulation of the Classical Friction Model for Motion Analysis and Simulation,'' Math. Comput. Modell., **5**, pp. 43–54.

[15] Yang, S., and Tomizuka, M., 1988, ''Adaptive Pulse Width Control for Precise Pointing Under the Influence of Stiction and Coulomb Friction,'' ASME J. Dyn. Syst., Meas., Control, **110**, pp. 221–227.

[16] De Weerth, S. P., Nielsen, L., Mead, C. A., and Åström, K. J., 1991, ''A Simple Neuron Servo,'' IEEE Trans. Neural Netw., **2**, pp. 248–251.

[17] Popovic, M. R., Gorinevsky, D. M., and Goldenberg, A. A., 1995, ''Fuzzy Logic Controller for Accurate Pointing of Direct-Drive Mechanism Using Force Pulses,'' *IEEE Int. Conference on Robotics and Automation*, pp. 1166–1171.

[18] Hojjat, Y., and Higuchi, T., 1991, ''Application of Electromagnetic Impulsive Force to Precise Positioning,'' Int. J. Jpn. Soc. Precis. Eng., **25**, pp. 39–44.

[19] Futami, S., Furutani, A., and Yoshida, S., 1990, ''Nanometer Positioning and Its Micro-Dynamics,'' Nanotechnology, **1**, pp. 31–37.

[20] Ro, P. I., and Hubbel, P. I., 1993, ''Model Reference Adaptive Control of Dual-Mode Micro/Macro Dynamics of Ball Screws for Nanometer Motion,'' ASME J. Dyn. Syst., Meas., Control, **115**, pp. 103–108.

[21] Huang, S. J., Yen, J. Y., and Lu, S. S., 1999, ''Dual Mode Control of a System With Friction,'' IEEE Trans. Control Syst. Technol., **7**, pp. 306–314.

[22] Wu, R. H., and Tung, P. C., 2002, ''Studies of Stick-Slip Friction, Presliding Displacement and Hunting,'' ASME J. Dyn. Syst., Meas., Control, **124**, pp. 111–117.

[23] Polycarpou, A., and Soom, A., 1992, ''Transitions Between Sticking and Slipping, in Friction-Induced Vibration, Chatter, Squeal, and Chaos,'' *Proc. ASME Winter Annual Meeting*, New York, ASME, Volume DE-Vol. 49, pp. 139–148.

[24] Dupont, P., Hayward, V., Armstrong, B., and Altpeter, F., 2002, ''Single State Elasto-Plastic Friction Models,'' IEEE Trans. Autom. Control, **47**, pp. 787–792.